A spectral element-based phase field method for incompressible two-phase flows ⊘

Yao Xiao (肖姚); Zhong Zeng (曾忠) ✉; Liangqi Zhang (张良奇) ✉; ... et. al

Check for updates

CrossMark

View
Online

Export
Citation

Articles You May Be Interested In

A highly accurate bound-preserving phase field method for incompressible two-phase flows

Physics of Fluids (September 2022)

A high order spectral difference-based phase field lattice Boltzmann method for incompressible two-phase flows

Physics of Fluids (December 2020)

An improved multiphase lattice Boltzmann flux solver with phase interface compression for incompressible multiphase flows

Physics of Fluids (January 2023)
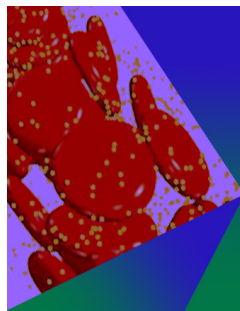
Physics of Fluids

Special Topic: Flow and Forensics

Submit Today!

AIP Publishing

AIP Publishing

A spectral element-based phase field method for incompressible two-phase flows

View Online   Export Citation   CrossMark

Yao Xiao (肖姚),[1] (iD) Zhong Zeng (曾忠),[1,a] (iD) Liangqi Zhang (张良奇),[1,a] (iD) Jingzhu Wang (王静竹),[2]
Yiwei Wang (王一伟),[2] (iD) Hao Liu (刘浩),[3] (iD) and Chenguang Huang (黄晨光)[2]

AFFILIATIONS

[1]College of Aerospace Engineering, Chongqing University, Chongqing 400044, People's Republic of China
[2]Key Laboratory for Mechanics in Fluid Solid Coupling Systems, Institute of Mechanics, Chinese Academy of Sciences,
  Beijing 100190, People's Republic of China
[3]Chongqing Southwest Research Institute for Water Transport Engineering, Chongqing Jiaotong University, Chongqing 400016,
  People's Republic of China

[a]Authors to whom correspondence should be addressed: zzeng@cqu.edu.cn and zhangliangqi@cqu.edu.cn

ABSTRACT

In this paper, we propose a spectral element-based phase field method by solving the Navier–Stokes/Cahn–Hilliard equations for incompressible two-phase flows. The high-order differential nonlinear term of the Cahn–Hilliard equation poses a great challenge for obtaining numerical solutions, so the Newton–Raphson method is adopted to tackle this conundrum. Furthermore, we employ the time-stepping scheme to decouple the Navier–Stokes equations to favor the computations with large density and viscosity contrast, in terms of both stability and convergence efficiency. In addition, the continuum surface tension model is used to account for the tangential component of the interfacial force, and thus our numerical method has the ability to simulate thermocapillary flows. We present four examples to demonstrate the interface capture accuracy of the proposed method. The shape of the rotating Zalesak's disk is accurately preserved by the present method even for two periods, which implies less dissipation and higher accuracy at long time numerical simulation. It is also noted that the present method with fourth-order element can achieve similar accuracy with the consistent scheme by evaluating the convective fluxes with the fifth-order weighted essentially non-oscillatory scheme. Moreover, the proposed method appears to comply well with mass conservation. And the results of thermocapillary flow test show good agreement with theoretical prediction. Finally, the rising bubble and Rayleigh–Taylor instability are considered to verify the proposed method for complex changes in interfacial topology, as well as its performance under large density and viscosity contrasts and high Reynolds number conditions.

Published under an exclusive license by AIP Publishing. https://doi.org/10.1063/5.0077372

I. INTRODUCTION

Multiphase flows are omnipresent in nature and industrial practice. In contrast to single-phase flows, multiphase flows are much more complex in the realm of computational fluid dynamics (CFD), owing to changes in the interface topology. Despite active research on this topic over the past years, viable methods to allow for accurate capture of dynamical interface under large fluid property contrast and high Reynolds number (Re) are still lacking.[1] Currently, multiphase flow methods can roughly be divided into two categories: interface tracking and interface capturing methods. The former tracks the interface explicitly through Lagrangian marker points, such as the front-tracking method,[2] the boundary integral method,[3] and the immersed boundary method.[4] The commonly used interface capturing method, including the volume of fluid (VOF) method,[5,6] level set method,[7] and

phase field method,[8,9] represents the interface implicitly in an Eulerian fashion through the evolution of an indicator function, which eases the solution of highly deformable interfacial dynamics. Particularly, the phase field method has gathered growing interest due to its favorable properties: (i) Its firm physical basis makes the governing equations derived therefrom consistent with the thermodynamic principles, and multi-physics process and various fluid properties can be incorporated readily via the energy-based variational formalism. (ii) Conservation laws (i.e., the mass and energy conservation) can also be preserved in theory.[10] (iii) The phase field method can effectively describe the complex interface changes without extra unphysical interface reconstruction process.

There has been a growing interest in developing multiphase flow methods based on the phase field model since the first attempt by

van der Waals.[11] Pioneering work also includes the fourth-order parabolic equation developed by Cahn and Hilliard,[12–14] i.e., the Cahn–Hilliard equation, to describe the spinodal decomposition of a two-phase flow, which can be regarded as a gradient flow problem. Nowadays, the Cahn–Hilliard equation has been widely used for diverse multiphase flow problems such as evaporation,[15] droplet coalescence and collision under electric field,[16] thermocapillary flows,[17] and so on.[18] Despite its success in various applications and the ongoing development, efficient and accurate phase field-based multiphase flow methods are still lacking.[1] The reason is that the high-order nonlinear diffusion term poses a great challenge for developing a numerical solution of the Cahn–Hilliard equation,[1] which makes the long-time computations difficult to converge to physically correct results. The situation becomes worse for simulations with large dimensionless mobility parameters[19,20] and large density and viscosity ratio.[21,22] At large Pe (Pe $= U_o \varepsilon / M_o$) numbers, the results of several models[23–25] show quantities of sawteeth along the interface and present many unphysical disturbances in the computational domain. Another difficulty is the numerical stability for long-time simulations of incompressible two-phase flows at high Re.[1] Researchers have put much effort in addressing the above challenges by using different strategies of usual second-order accuracy, such as the finite volume method,[17,26] finite element method,[27] and lattice Boltzmann method.[28,29]

Essential progress has also been made by applying the high-order schemes to reduce dissipation and improve accuracy. Moreover, as claimed by Shen et al., in contrast to common second-order numerical methods (such as the finite difference method), the spectral method with exponential convergence can effectively save computation costs at the same accuracy level.[30,31] Shi and Li[32] developed a local discontinuous Galerkin method with implicit–explicit multistep time-mapping to solve the Cahn–Hilliard equation. Park et al.[33] proposed a least squares spectral element method with a time-stepping procedure, a high-order continuity approximation, and an element-by-element solver technique to the isothermal Navier–Stokes/Cahn–Hilliard system. Manzanero et al.[34,35] presented a nodal discontinuous Galerkin spectral element method for the Cahn–Hilliard equation and developed an entropy-stable incompressible two-phase flow solver. Ma et al.[29] proposed a high-order spectral difference-based phase field lattice Boltzmann method for incompressible two-phase flows. Shen and Yang[36,37] came up with a pressure stabilization scheme for two-phase flows under large density contrast, which is widely used in the context of Galerkin finite elements and Galerkin-spectral methods. An efficient time-stepping scheme was developed by Dong and Shen[21] for large-density ratio problems within the spectral element method framework, which has been extended to thermal two-phase flows without considering the thermocapillary effects.[38]

In this work, we propose a spectral element-based phase field method for incompressible two-phase flows with large density and viscosity contrast and at high Re. The Newton–Raphson method is adopted to resolve the Cahn–Hilliard equation, and the application of time-stepping scheme[36] for the Navier–Stokes equations aims to warrant stability and convergence efficiency of the simulations with large fluid property contrast. Furthermore, the continuum surface force (CSF) model extended for the phase field method[39] is used to represent the interfacial force and include the tangential component of surface tension. We validate the proposed two-phase flow method by a series of tests, including the Zalesak's disk rotation, reversed single

vortex flow, bubbles merging, thermocapillary flows in a heated microchannel, as well as rising bubble and Rayleigh–Taylor instability. The interface capture accuracy, as well as the mass conservation property, is quantitatively verified by the first four examples. Numerical results for the last two tests prove the robustness and accuracy for complex changes in the interfacial topology under large fluid property contrast and high Re.

II. THEORY AND ALGORITHM
A. Governing equations

The phase field method involves a sharp interface with a diffuse layer of thickness ε. For immiscible two-phase flows, the order parameter ϕ is used to label the disparate phases: $\phi = 1$ and -1 correspond to fluid 1 and fluid 2, respectively. The evolution of the order parameter is governed by the convective Cahn–Hilliard equation given by[39]

$$\frac{\partial \phi}{\partial t} + \mathbf{u} \cdot \nabla \phi = \nabla \cdot (M_0 \nabla \psi), \quad (1)$$

where $\mathbf{u}$ is the velocity. M_0 is the mobility, which characterizes the diffusivity in the interfacial region. ψ is the chemical potential, which is derived from the variation of free energy.

$$\psi = \frac{\delta F}{\delta \phi} = (\phi^2 - 1)\phi - \varepsilon^2 \nabla^2 \phi. \quad (2)$$

The total free energy F reads as follows:

$$F(\phi) = \int_\Omega \left(f_{dw}(\phi) + \frac{\varepsilon^2}{2} |\nabla \phi|^2 \right) d\Omega, \quad (3)$$

where Ω represents the fluid domain. The first term of the integrand stands for the bulk free energy density, and follows a double-well form $f_{dw}(\phi) = (\phi^2 - 1)^2/4$. The second term accounts for the excess free energy in the interfacial region. At equilibrium, the profile along the z axis for a one-dimensional planar interface is expressed as follows:

$$\phi(z) = \tanh\left(\frac{z}{\sqrt{2}\varepsilon} \right). \quad (4)$$

Based on the phase field method, we have assumed for simplicity that, if the fluid interface intersects with the wall, the contact angle would be 90°. The boundary conditions for the phase field equation are expressed as follows:[21]

$$\mathbf{n}_w \cdot \nabla \phi = 0 \quad \mathbf{n}_w \cdot \nabla \psi = 0. \quad (5)$$

The interfacial force formula proposed by Liu et al.[39,40] includes the tangential component as follows:

$$\mathbf{f}_\sigma = \frac{3\sqrt{2}}{4} \varepsilon \left[|\nabla \phi|^2 \nabla \sigma - (\nabla \sigma \cdot \nabla \phi)\nabla \phi + \frac{\sigma}{\varepsilon^2} \psi \nabla \phi \right], \quad (6)$$

where the σ is the local surface tension parameter. In this context, its linear dependency on the temperature results in the thermocapillary effect, i.e.,

$$\sigma = \sigma_0 - \sigma_T (T - T_0), \quad (7)$$

where σ_0 is the surface tension at the reference temperature T_0 and σ_T denotes the change rate of the surface tension with T. For isothermal cases, the expression for surface tension reduces to

$$\mathbf{f}_\sigma = \frac{3\sqrt{2}}{4}\frac{\sigma}{\varepsilon}\psi\nabla\phi. \tag{8}$$

Having in mind the relation in Eq. (7), the governing equations for incompressible two-phase flows read as follows:

$$\rho\left(\frac{\partial \mathbf{u}}{\partial t} + \mathbf{u}\cdot\nabla\mathbf{u}\right) = -\nabla p + \nabla\cdot\left[\mu\left(\nabla\mathbf{u} + (\nabla\mathbf{u})^{\mathrm{T}}\right)\right] + \mathbf{f}_\sigma + \rho\mathbf{g}, \tag{9}$$

$$\nabla\cdot\mathbf{u} = 0, \tag{10}$$

$$\begin{cases} \dfrac{\partial \phi}{\partial t} + \mathbf{u}\cdot\nabla\phi = \nabla\cdot(M\nabla\psi), \\ \psi = (\phi^2 - 1)\phi - \varepsilon^2\nabla^2\phi, \end{cases} \tag{11}$$

$$\rho c_p\left(\frac{\partial T}{\partial t} + \mathbf{u}\cdot\nabla T\right) = \nabla\cdot(\kappa\nabla T), \tag{12}$$

where $\mathbf{g}$ is the acceleration due to gravity. The fluid properties including the density ρ, dynamic viscosity μ, specific heat c_p, and thermal conductivity κ are determined from the phase field parameter as follows:

$$\rho = \frac{\rho_1 + \rho_2}{2} + \frac{\rho_1 - \rho_2}{2}\phi, \quad \mu = \frac{\mu_1 + \mu_2}{2} + \frac{\mu_1 - \mu_2}{2}\phi, \tag{13}$$

$$c_p = \frac{c_{p1} + c_{p2}}{2} + \frac{c_{p1} - c_{p2}}{2}\phi, \quad \kappa = \frac{\kappa_1 + \kappa_2}{2} + \frac{\kappa_1 - \kappa_2}{2}\phi. \tag{14}$$

B. The algorithm

In this section, a spectral element method for two-phase flows is proposed by solving Eqs. (9)–(12). We use the time-stepping scheme[21,38] to decouple the Navier–Stokes equation into two Poisson-type equations and to construct a constant stiffness coefficient for the Navier–Stokes equation, which overcomes the performance bottleneck caused by variable coefficient matrices associated with variable density and variable viscosity. Moreover, the Newton–Raphson method[41] is incorporated for the Cahn–Hilliard equation. Let ϕ^n, $\mathbf{u}^n$, p^n, and T^n denote the phase, velocity, pressure, and temperature field at time step n, respectively. To obtain the flow variables at time step $(n+1)$, we solve for the phase parameter, the temperature, the pressure, and velocity sequentially as follows:

For phase field ϕ^{n+1},

$$\begin{cases} \dfrac{\gamma_0\phi^{n+1}}{\Delta t} + \mathbf{u}^{*,n+1}\cdot\nabla\phi^{n+1} - \nabla\cdot(M\nabla\psi^{n+1}) = \dfrac{\hat{\phi}}{\Delta t}, \\ \varepsilon^2\nabla^2\phi^{n+1} - \left[(\phi^{n+1})^2 - 1\right]\phi^{n+1} + \psi^{n+1} = 0. \end{cases} \tag{15}$$

For temperature T^{n+1},

$$\frac{\gamma_0 T^{n+1}}{\Delta t} + \mathbf{u}^{*,n+1}\cdot\nabla T^{n+1} - a_m\nabla^2 T^{n+1}$$
$$= \left(\frac{\kappa^{n+1}}{\rho^{n+1}c^{n+1}} - a_m\right)\nabla^2 T^{*,n+1} + \frac{1}{\rho^{n+1}c^{n+1}}\nabla\kappa^{n+1}\cdot\nabla T^{*,n+1} + \frac{\hat{T}}{\Delta t}. \tag{16}$$

For pressure p^{n+1},

$$\gamma_0\tilde{\mathbf{u}}^{n+1}1 - \frac{\hat{\mathbf{u}}}{\Delta}t + \frac{1}{\rho_0}\nabla p^{n+1}$$

$$= -(\mathbf{u}^{*,n+1}\cdot\nabla)\mathbf{u}^{*,n+1} + \left(\frac{1}{\rho_0} - \frac{1}{\rho^{n+1}}\right)\nabla p^{*,n+1} - \frac{\mu^{n+1}}{\rho^{n+1}}\nabla\times\nabla\times\mathbf{u}^{*,n+1}$$

$$+ \frac{1}{\rho^{n+1}}\nabla\mu^{n+1}\cdot\left[\nabla\mathbf{u}^{*,n+1} + (\nabla\mathbf{u}^{*,n+1})^{\mathrm{T}}\right] + \frac{1}{\rho^{n+1}}\mathbf{f}_\sigma + \mathbf{g}, \tag{17}$$

$$\nabla\cdot\tilde{\mathbf{u}}^{n+1}1 = 0, \tag{18}$$

$$\mathbf{n}\cdot\tilde{\mathbf{u}}^{n+1}1|_\Gamma = \mathbf{n}\cdot\mathbf{w}^{n+1}. \tag{19}$$

For velocity $\mathbf{u}^{n+1}$,

$$\frac{\gamma_0\mathbf{u}^{n+1}}{\Delta t} - \nu_m\nabla^2\mathbf{u}^{n+1} = \frac{\gamma_0\tilde{\mathbf{u}}^{n+1}1}{\Delta t} + \nu_m\nabla\times\nabla\times\mathbf{u}^{*,n+1}, \tag{20}$$

where $\frac{\gamma_0\tilde{\mathbf{u}}^{n+1}1}{\Delta t}$ is calculated from Eq. (17) as follows:

$$\frac{\gamma_0\tilde{\mathbf{u}}^{n+1}1}{\Delta t} = \frac{\hat{\mathbf{u}}}{\Delta}t - \frac{1}{\rho_0}\nabla p^{n+1} - (\mathbf{u}^{*,n+1}\cdot\nabla)\mathbf{u}^{*,n+1} + \left(\frac{1}{\rho_0} - \frac{1}{\rho^{n+1}}\right)$$

$$\times \nabla p^{*,n+1} - \frac{\mu^{n+1}}{\rho^{n+1}}\nabla\times\nabla\times\mathbf{u}^{*,n+1}$$

$$+ \frac{1}{\rho^{n+1}}\nabla\mu^{n+1}\cdot\left[\nabla\mathbf{u}^{*,n+1} + (\nabla\mathbf{u}^{*,n+1})^{\mathrm{T}}\right] + \frac{1}{\rho^{n+1}}\mathbf{f}_\sigma + \mathbf{g}, \tag{21}$$

$$\mathbf{u}^{*,n+1} = 2\mathbf{u}^n - \mathbf{u}^{n-1}, \tag{22}$$

$$\mathbf{u}^{n+1}|_\Gamma = \mathbf{w}^{n+1}, \tag{23}$$

where Δt is the time step. For stability reasons, the constant parameters ν_m, ρ_0, a_m fulfill the following requirements:

$$\nu_m \geq \frac{1}{2}\frac{\max(\mu_1, \mu_2)}{\min(\rho_1, \rho_2)}, \quad \rho_0 = \min(\rho_1, \rho_2),$$

$$a_m \geq \frac{1}{2}\frac{\max(\kappa_1, \kappa_2)}{\min(\rho_1, \rho_2)\min(c_1, c_2)}.$$

The present scheme introduces a time-independent constant coefficient matrix by adding $\frac{1}{\rho_0}\nabla p^{n+1}$ and its correction term $\left(\frac{1}{\rho_0} - \frac{1}{\rho^{n+1}}\right)\nabla p^{*,n+1}$ in Eq. (17) and by adding $\nu_m\nabla^2\mathbf{u}^{n+1}$ and its correction term $\nu_m\nabla\times\nabla\times\mathbf{u}^{*,n+1}$ in Eq. (20).[21,42,43] For generality, we use χ to represent $\mathbf{u}$ and ϕ. Then, $\chi^{*,n+1}$ represents a Jth-order (J is the order of temporal accuracy, J = 1 or 2) explicit approximation of χ^{n+1} as follows:

$$\chi^{*,n+1} = \begin{cases} \chi^n & \text{if } J = 1, \\ 2\chi^n - \chi^{n-1} & \text{if } J = 2. \end{cases} \tag{24}$$

The expression $(\gamma_0\tilde{\chi}^{n+1} - \hat{\chi})/\Delta t$ is a discretization of $\frac{\partial \chi}{\partial t}$ at time step $(n+1)$ with the Jth-order backward differentiation formula, where

$$\gamma_0 = \begin{cases} 1 & \text{if } J = 1, \\ \dfrac{3}{2} & \text{if } J = 2. \end{cases} \qquad \hat{\chi} = \begin{cases} \chi^n & \text{if } J = 1, \\ 2\chi^n - \dfrac{1}{2}\chi^{n-1} & \text{if } J = 2. \end{cases} \tag{25}$$

Here, we discuss the implementation of this scheme by employing a spectral element method discretization in space. First of all, we take consideration of ϕ^n with the Newton–Raphson method.[41] Take the L^2-inner product of Eq. (15) with q and ζ for ϕ and ψ, respectively; we obtain the weak form of Eq. (15) as follows:

$$\begin{cases} \int_\Omega \left(\dfrac{\gamma_0 \phi^{n+1}}{\Delta t} + \mathbf{u}^{*,n+1} \cdot \nabla \phi^{n+1} \right) q + \int_\Omega M \nabla \psi^{n+1} \cdot \nabla q = \int_\Omega \dfrac{\hat{\phi}}{\Delta t} q, \\ \int_\Omega \varepsilon^2 \nabla \phi^{n+1} \cdot \nabla \zeta + \int_\Omega \left[(\phi^{n+1})^2 - 1 \right] \phi^{n+1} \zeta - \int_\Omega \psi^{n+1} \zeta = 0. \end{cases} \quad (26)$$

Spatial discretization based on the spectral element method is introduced in the Appendix. According Eqs. (A7)–(A16) and Eq. (26), the residual vector can be expressed as follows:

$$R_1 = \sum_{j=0}^{N_\xi} \sum_{k=0}^{N_\eta} \left(\dfrac{\gamma_0 \phi^{n+1}}{\Delta t} B_{jkmn} + u^{*,n+1} \phi^{n+1} N^x_{jkmn} \right.$$
$$\left. + v^{*,n+1} \phi^{n+1} N^y_{jkmn} + M \psi^{n+1} A_{jkmn} - \dfrac{\hat{\phi}}{\Delta t} B_{jkmn} \right), \quad (27)$$

$$R_2 = \sum_{j=0}^{N_\xi} \sum_{k=0}^{N_\eta} \left(\varepsilon^2 \phi^{n+1} A_{jkmn} + \left[(\phi^{n+1})^2 - 1 \right] \phi^{n+1} B_{jkmn} - \psi^{n+1} B_{jkmn} \right). \quad (28)$$

Accordingly, we define the Jacobian matrix as follows:

$$\mathbf{J} = \begin{pmatrix} \dfrac{\partial R_1}{\partial \phi^{n+1}} & \dfrac{\partial R_1}{\partial \psi^{n+1}} \\ \dfrac{\partial R_2}{\partial \phi^{n+1}} & \dfrac{\partial R_2}{\partial \psi^{n+1}} \end{pmatrix}, \quad (29)$$

where

$$\dfrac{\partial R_1}{\partial \phi^{n+1}} = \sum_{j=0}^{N_\xi} \sum_{k=0}^{N_\eta} \left(\dfrac{\gamma_0}{\Delta t} B_{jkmn} + u^{*,n+1} N^x_{jkmn} + v^{*,n+1} N^y_{jkmn} \right), \quad (30)$$

$$\dfrac{\partial R_1}{\partial \psi^{n+1}} = \sum_{j=0}^{N_\xi} \sum_{k=0}^{N_\eta} (M A_{jkmn}), \quad (31)$$

$$\dfrac{\partial R_2}{\partial \phi^{n+1}} = \sum_{j=0}^{N_\xi} \sum_{k=0}^{N_\eta} \left(\varepsilon^2 A_{jkmn} + (3\phi^2 - 1) B_{jkmn} \right), \quad (32)$$

$$\dfrac{\partial R_2}{\partial \psi^{n+1}} = \sum_{j=0}^{N_\xi} \sum_{k=0}^{N_\eta} (-B_{jkmn}). \quad (33)$$

After formulating the residuals and the Jacobian matrix, they are assembled into the global stiffness and right-hand side vectors. The resulting set of nonlinear equations is

$$[J]\{d\delta\} = \{R^G\}, \quad (34)$$

where $R^G = (R_1, R_2)^T$ and $d\delta = (d\phi_1, d\phi_2, \ldots, d\phi_N, d\psi_1, d\psi_2, \ldots d\psi_N)^T$, N being the total number of nodes in spectral element mesh. At each time increment step, we propose to solve the nonlinear equation in Eq. (34) iteratively with the modified Newton–Raphson scheme to gain computational efficiency. In the present Newton–Raphson algorithm, the left-hand Jacobian matrix $\mathbf{J}$ is formed only once at the beginning of each time step. In the following iteration steps, the residual vector, R^G, is re-evaluated and Eq. (34) is then solved again to update $\delta^{n+1} = \delta^n + d\delta$. This iterative solution process continues until the prescribed accuracy criterion (err $= 1 \times 10^{-6}$) is reached.

After the phase field ϕ^{n+1} and chemical potential ψ^{n+1} are obtained, we can update ρ, μ, c_p, and κ. For obtaining the pressure and velocity, we set

$$G_p = \dfrac{\hat{\mathbf{u}}}{\Delta} t - (\mathbf{u}^{*,n+1} \cdot \nabla) \mathbf{u}^{*,n+1} + \left(\dfrac{1}{\rho_0} - \dfrac{1}{\rho^{n+1}} \right) \nabla p^{*,n+1}$$
$$+ \dfrac{1}{\rho^{n+1}} \nabla \mu^{n+1} \cdot \left[\nabla \mathbf{u}^{*,n+1} + (\nabla \mathbf{u}^{*,n+1})^{\mathrm{T}} \right] + \dfrac{1}{\rho^{n+1}} \mathbf{f}_\sigma + \mathbf{g}. \quad (35)$$

Taking the L^2-inner product of Eq. (17) with ∇h, we can acquire the Poisson equation for the weak form of pressure p^{n+1} as follows:

$$\int_\Omega \nabla p^{n+1} \cdot \nabla h = \rho_0 \int_\Omega \left[\mathbf{G} + \nabla \left(\dfrac{\mu^{n+1}}{\rho^{n+1}} \right) \times \omega^{*,n+1} \right]$$
$$\cdot \nabla h - \rho_0 \int_\Gamma \dfrac{\mu^{n+1}}{\rho^{n+1}} \mathbf{n} \times \omega^{*,n+1} \cdot \nabla h$$
$$- \dfrac{\gamma_0 \rho_0}{\Delta t} \int_\Gamma \mathbf{n} \cdot \mathbf{w}^{n+1} h, \quad \forall q \in H^1(\Omega), \quad (36)$$

where

$$\dfrac{\mu^{n+1}}{\rho^{n+1}} \nabla \times \omega \cdot \nabla h = \nabla \cdot \left(\dfrac{\mu}{\rho} \omega \times \nabla h \right) - \nabla \left(\dfrac{\mu}{\rho} \right) \times \omega^{*,n+1} \cdot \nabla h. \quad (37)$$

According to Eqs. (20)–(23), we set

$$\mathbf{G}_u = \mathbf{g} + \dfrac{\hat{\mathbf{u}}}{\Delta t} + \dfrac{1}{\rho^{n+1}} \mathbf{f}_\sigma + \dfrac{1}{\rho^{n+1}} \nabla \mu^{n+1} \cdot \left[\nabla \mathbf{u}^{*,n+1} + (\nabla \mathbf{u}^{*,n+1})^{\mathrm{T}} \right]$$
$$+ \left(\dfrac{1}{\rho_0} - \dfrac{1}{\rho^{n+1}} \right) \nabla p^{*,n+1} - (\mathbf{u}^{*,n+1} \cdot \nabla) \mathbf{u}^{*,n+1}$$
$$+ \nabla \left(\dfrac{\mu^{n+1}}{\rho^{n+1}} \right) \times \omega^{*,n+1}. \quad (38)$$

Also, the weak form of velocity is given by

$$\dfrac{\gamma_0}{\nu_m \Delta t} \int_\Omega \mathbf{u}^{n+1} h + \int_\Omega \nabla h \cdot \nabla \mathbf{u}^{n+1}$$
$$= \dfrac{1}{\nu_m} \int_\Omega h \left(\mathbf{G} - \dfrac{1}{\rho_0} \nabla p^{n+1} \right) - \dfrac{1}{\nu_m} \int_\Omega \left(\dfrac{\mu^{n+1}}{\rho^{n+1}} - \nu_m \right) \omega^{*,n+1}$$
$$\times \nabla h - \dfrac{1}{\nu_m} \int_\Gamma \left(\dfrac{\mu^{n+1}}{\rho^{n+1}} - \nu_m \right) \mathbf{n} \times \omega^{*,n+1} h, \quad \forall h \in H_0^1(\Omega). \quad (39)$$

Taking advantage of the Legendre–Gauss–Lobatto nodes, a non-uniform grid based on the Legendre–Gauss–Lobatto nodes was used. In practice, the temperature Helmholtz equation (16), the pressure Poisson equation (36), and the velocity Helmholtz equation (39) are all solved by the Legendre spectral element method as shown in the Appendix.

III. INTERFACE CAPTURE ACCURACY VALIDATION

In this section, we present four numerical examples for comprehensive validation of the proposed two-phase flow method in terms of interface capture accuracy. The solution accuracy for the Cahn–Hilliard equation is evaluated by the first two tests, i.e., the Zalesak's disk

problem and reversed single vortex flow with prespecified velocity field. The bubbles merging test is used for the verification of mass conservation of the present method. The last test is devoted to prove its validity for thermocapillary flows.

A. Zalesak's disk rotation

The Zalesak's disk is a classic test to assess the interface capture accuracy. Theoretically, the rotating disk will return to its initial position after each period $\tau = 2L/U_0$. A grooved disk with radius R is initially located in the center of a square with side length L (200 m), as shown in Fig. 1. The computational domain is resolved by 2500 quadrilateral elements (50 elements in the x- and y-directions) with various elemental orders. In the computation, the width of the groove is 0.08 L, the interface width $\varepsilon = 0.01$ L, the time step $\Delta t = 2$ s, the Courant number $CFL = u\Delta t/\Delta x \approx 0.1$, and the radius of the groove $R = 0.4$ L. The dimensionless parameter Pe is defined as $Pe = U_o\varepsilon/M_o$.[44] The analytical velocity field for the present test is given by

$$u = -U_0\pi\left(\frac{y}{L} - 0.5\right), \quad v = U_0\pi\left(\frac{x}{L} - 0.5\right). \quad (40)$$

To quantitatively compare with the reference results,[19,20,29] the relative error E_ϕ is defined in terms of the phase parameter as

$$E_\phi = \frac{\sum_{\mathbf{X}}|\phi(\mathbf{X}, n\tau) - \phi(\mathbf{X}, 0)|}{\sum_{\mathbf{X}}|\phi(\mathbf{X}, 0)|}, \quad (41)$$

where $\phi(\mathbf{X}, n\tau)$ is the phase variable distribution after n periods and $\phi(\mathbf{X}, 0)$ is its initial value. Table I tabulates the relative errors E_ϕ vs different elemental orders for the case Pe = 800 ($M_0 = 0.0001$ and $U_0 = 0.04$ m/s). E_ϕ decreases with the increment of element order especially from 3 to 4 and remains unchanged on further increasing the element order. Therefore, the element order 4 is adopted by default for the remaining tests. To test for mesh convergence, we demonstrate the relative error E_ϕ of the current problem in Table II. Moreover, Table III compares relative errors E_ϕ from the present scheme against the reference results after one period. Obviously, the proposed scheme is much more accurate than the reference results from the lattice Boltzmann method (LBM) based on both the Cahn–Hilliard equation
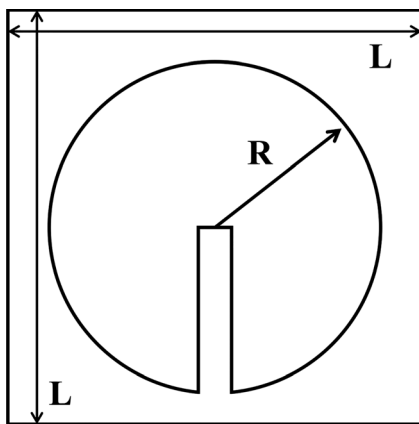

FIG. 1. Initial setup for Zalesak's disk.

TABLE I. Relative errors of the present model under different element orders for the problem of Zalesak's disk.

Element order	Relative error
N = 2	0.0369
N = 3	0.0357
N = 4	0.0141
N = 5	0.0141

and the Allen–Cahn equation under the same mesh resolution. In addition, the present method exhibits higher accuracy than the hybrid spectral difference LBM, which uses the same element order 4 but a higher mesh resolution (6400 quadrilateral elements). Moreover, the present scheme is relatively insensitive to the mobility coefficient for both test cases, while the reported works[19,20] with second-order accuracy are heavily affected. Figure 2 gives the shape of the phase interface at different times for the Pe = 800 case. The numerical results at different times fit well with the initial profile of the disk. An important point to note is that even after two periods, the results from the present method match well with the initial shape [Fig. 2(e)] and the relative error E_ϕ is 0.0220, which is also much better than the reported results. Table IV shows the relative error E_ϕ of the present model under ten periods at Pe = 800. E_ϕ rapidly increases at first and gradually flattens out. The above results indicate that the proposed method can provide convergent results for computations with large Pe numbers, while the model in Ref. 19 becomes unstable at Pe = 800 under the same mesh resolution.

B. Reversed single vortex flow

We consider the single vortex flow to further verify the convergence and interface capture accuracy of the present method.[19,22] Driven by the given time-dependent velocity field, the interface deforms drastically and exhibits strong nonlinear features. The interface will gradually form an arc shape in the first half-period, and reach the maximum deformation at $\tau/2$, and then return to the original shape in the next half-period. At τ, the circular disk will get back to its initial position with its shape unchanged in theory. Figure 3 is a schematic diagram of the computational domain $\Omega = [0, L] \times [0, L]$, which is a square with a side length L. The mesh resolution of 241 × 241 (60 elements in the x- and y-directions and element order 4 in each element) is adopted in this calculation. Initially, a circular disk with radius R is placed at (x_0, y_0), and the unsteady velocity field is given by

TABLE II. Relative errors of the present model under different element numbers for the problem of Zalesak's disk.

Element number	Relative error
12 × 12	0.0376
25 × 25	0.0221
50 × 50	0.0141
75 × 75	0.0141

TABLE III. Relative errors of the present model and three literature studies[19,20,29] for the problem of Zalesak's disk.

M_0	$U_0 = 0.02$				$U_0 = 0.04$			
	Present	AC[20]	CH[19]	CH[29]	Present	AC[20]	CH[19]	CH[29]
0.01	0.0204	0.0269	0.0421	· · ·	0.0138	0.0266	0.0485	· · ·
0.001	0.0139	0.0414	0.0554	· · ·	0.0141	0.0409	0.0696	· · ·
0.0001	0.0141	0.0434	0.0953	0.0209	0.0141	0.0491	· · ·	0.0276
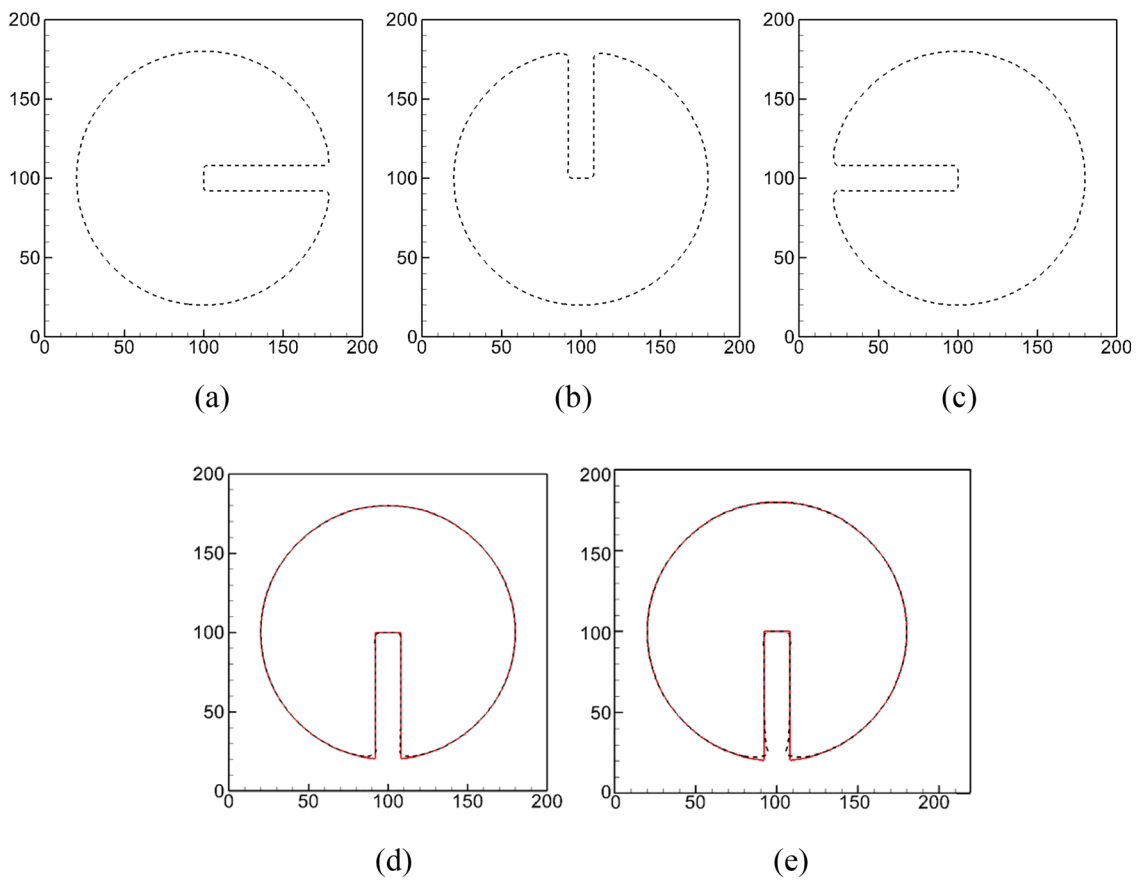
FIG. 2. Phase interface ($\phi = 0$) at different times when Pe = 800 (the red solid line is the initial value, and the black dashed line is the numerical solution): (a) $t = \tau/4$, (b) $t = \tau/2$, (c) $t = 3\tau/4$, (d) $t = \tau$, and (e) $t = 2\tau$.

TABLE IV. Relative errors E_ϕ of the present model for the problem of Zalesak's disk after multiple periods at Pe = 800.

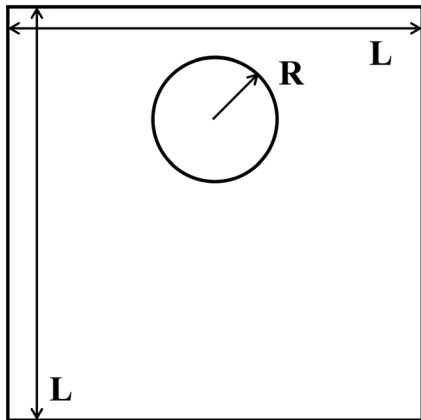| Number of periods	1	2	3	4	5	6	7	8	9	10
E_ϕ	0.0141	0.0220	0.0278	0.0324	0.0362	0.0394	0.0422	0.0447	0.0469	0.0489

FIG. 3. Schematic diagram of the single vortex flow.

$$u = -U_0 \sin^2 \frac{\pi x}{L} \sin \frac{\pi y}{L} \cos \frac{\pi y}{L} \cos \frac{\pi t}{\tau},$$
$$v = U_0 \sin \frac{\pi x}{L} \sin^2 \frac{\pi y}{L} \cos \frac{\pi x}{L} \cos \frac{\pi t}{\tau}, \qquad (42)$$

where t is the time, $U_0 = 1$ m/s, $L = 1$ m, $R = 0.3L$ m, $x_0 = 0.5L$ m, $y_0 = 0.75L$ m, $M_0 = 1 \times 10^{-4}$, the time step $\Delta t = 5 \times 10^{-4}$ s, and $\tau = 2$ s, which follows the case setup in Ref. 22. We define the following L_2 error to compare our results with those by Huang *et al*:[22]

$$Er = r - \sqrt{(x_t - x_0)^2 + (y_t - y_0)^2}, \qquad (43)$$

where (x_t, y_t) is the coordinate point of $\phi = 0$ at different times. Figure 4 tabulates the L_2 error from the present method in comparison with the reference results for different elemental numbers, i.e., 36, 144, 625, and 2500. With increase in the mesh resolution, the L_2 error reduces obviously. For the same mesh resolution, the proposed method of element order 4 exhibits fewer errors than the consistent method by resolving the convective flux with the fifth-order weighted
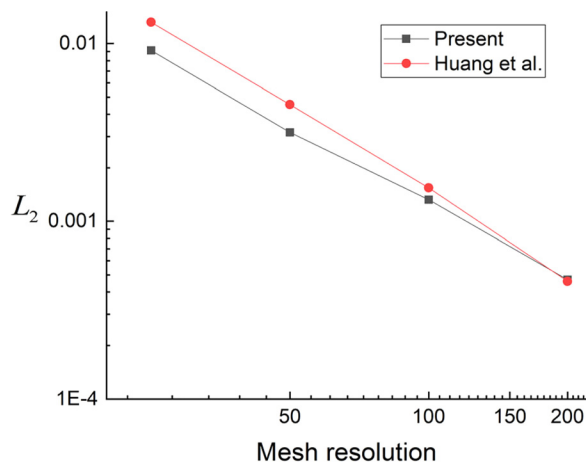

FIG. 4. L_2 error of the single vortex flow.

essentially non-oscillatory scheme.[22] Figure 5 shows the interface evolution in one periodic time with four sets of different grids, i.e., grid with 6×6, 12×12, 25×25, and 50×50 elements for case A, case B, case C, and case D, respectively. As the mesh resolution increases, the disk matches better with the initial shape after one period.

C. Bubbles merging

A test of the fusion of two bubbles with more deformable interface is performed to verify the conservation characteristic of the present method. As indicated in the previous study,[45] coalescence occurs when the shortest distance between two bubbles is less than 2ε, and the radii of the merged bubble R_T and the initial bubble R_0 follow the correlation $R_T = \sqrt{2}R_0$, which is only true for coalescence of identically sized bubbles. The computational domain $\Omega = [0, L] \times [0, L]$, as shown in Fig. 6, is covered by 2500 quadrilateral elements (50 elements in both x- and y-direction) here. Two bubbles with radius R_0 are initially located at $(-22.5, 0)$ and $(22.5, 0)$, respectively. The width of the interface is $\varepsilon = 0.13 R_0$, and the interface distance $d = 0.125 R_0$. The other flow parameters are set as follows: $\rho_1 = 1$ kg/m³, $\rho_2 = 10$ kg/m³, $\mu_1 = 0.1$ Pa · s, $\mu_2 = 0.1$ Pa · s, $\sigma = 0.01$ N/m, $M_0 = 0.001$, $\Delta t = 1$ s, $L = 120$ m, and $R_0 = 20$ m. Figure 7 demonstrates the fusion process of two bubbles, and the two bubbles slowly merged and finally formed a larger bubble. As in Fig. 7(i), the merged bubble becomes stable and its radius R_T accords well with the theoretical prediction. For quantitative analysis, the relative error is defined as follows:

$$E_r = \frac{|R_T - \sqrt{2}R_0|}{\sqrt{2}R_0}. \qquad (44)$$

The results from the present method correspond to a relative error less than 0.2%, while the relative error in Refs. 46 and 29 is 8.42% and the relative error in Refs. 26 and 47 is 3.81%. We note that the deviation from theoretical prediction, i.e., the relative error in Eq. (44), reflects the performance of the two-phase flow method in preserving mass conservation. Therefore, the proposed two-phase flow method outperforms the reference method in complying with mass conservation, which can be attributed to the lower dissipation and higher interface capture accuracy of the present method.

D. Thermocapillary flows in a heated microchannel with two superimposed fluids

The thermocapillary flow in a heated microchannel with two superimposed fluids is finally simulated in this section. As sketched in Fig. 8, the heights of the upper fluid 1 and the lower fluid 2 are a and b, respectively. The length of the domain in the x-direction is L. We, respectively, impose a sinusoidal temperature on the bottom wall, i.e.,

$$T(x, -b) = T_h + T_0 \cos(\omega x) \qquad (45)$$

and a uniform temperature on the top wall, i.e.,

$$T(x, a) = T_c, \qquad (46)$$

where $0 < T_0 < T_c < T_h$ and $\omega = \frac{2\pi}{L_c}$ denotes the wavenumber.

The characteristic length and velocity for the present test are $L_c = b$ and $U = L^{-1} b \sigma_T T_0 / \mu_2$, respectively. The dimensionless parameters, i.e., the Reynolds Re, Marangoni Ma, and capillary number Ca, read as follows:
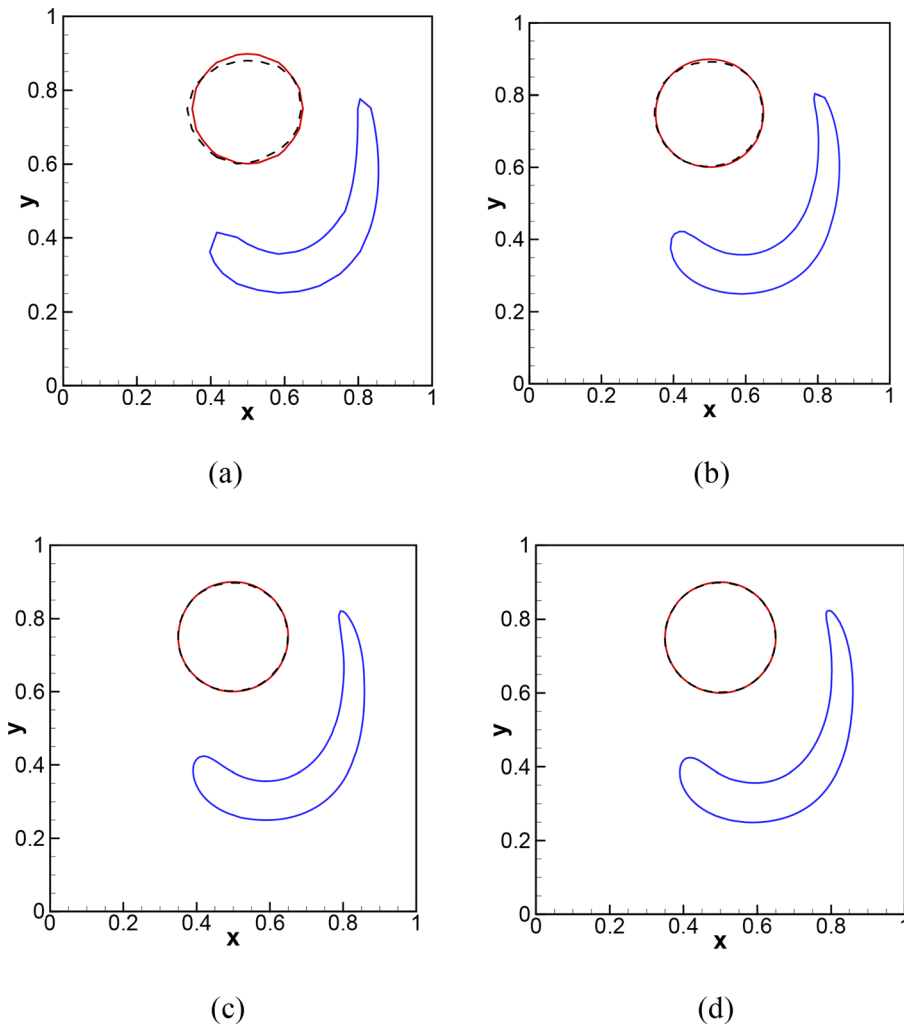
FIG. 5. Interface evolution in time obtained from various mesh resolutions (the red solid line denotes the initial profile at $t = 0$, the blue solid lines are results at $t = \tau/2$, and the black dashed lines are the results at $t = \tau$): (a) case A, (b) case B, (c) case C, and (d) case D.
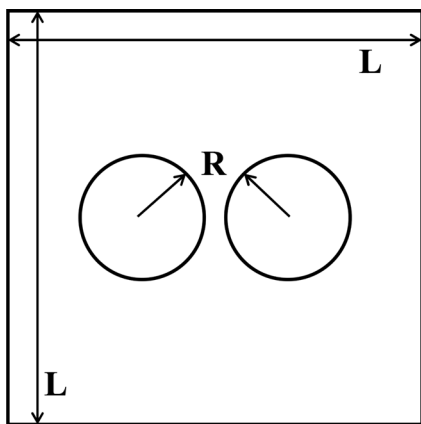
FIG. 6. Schematic diagram of bubbles merging.

$$\mathrm{Re} = \frac{\rho_2 L_c U}{\mu_2}, \quad \mathrm{Ma} = \frac{\rho_2 c_{p2} L_c U}{\kappa_2}, \quad \mathrm{Ca} = \frac{U \mu_2}{\sigma_0}. \quad (47)$$

The convective transport of momentum and energy is quite limited when the above parameters are negligibly small, and the interface remains flat. The analytical solutions[48] yield the stream function $\bar{\Psi}(x, y)$ and temperature distribution $\bar{T}(x, y)$ as follows:

$$\bar{\psi}(x, y) = \frac{U_{\max}}{\omega} \frac{1}{\sinh^2(\alpha) - \alpha^2} \Big\{ \omega y \sinh^2(\alpha) \cosh(\omega y)$$
$$- 0.5 \big[2\alpha^2 + \omega y (\sinh(2\alpha) - 2\alpha) \big] \sinh(\omega y) \Big\} \sin(\omega x), \quad (48)$$

$$\bar{T}(x, y) = \frac{(T_c - T_h) y + \tilde{\kappa} T_c b + T_h a}{a + \tilde{\kappa} b}$$
$$+ T_0 f(\alpha, \beta, \tilde{\kappa}) \sinh(\alpha - \omega y) \cos(\omega x) \quad (49)$$
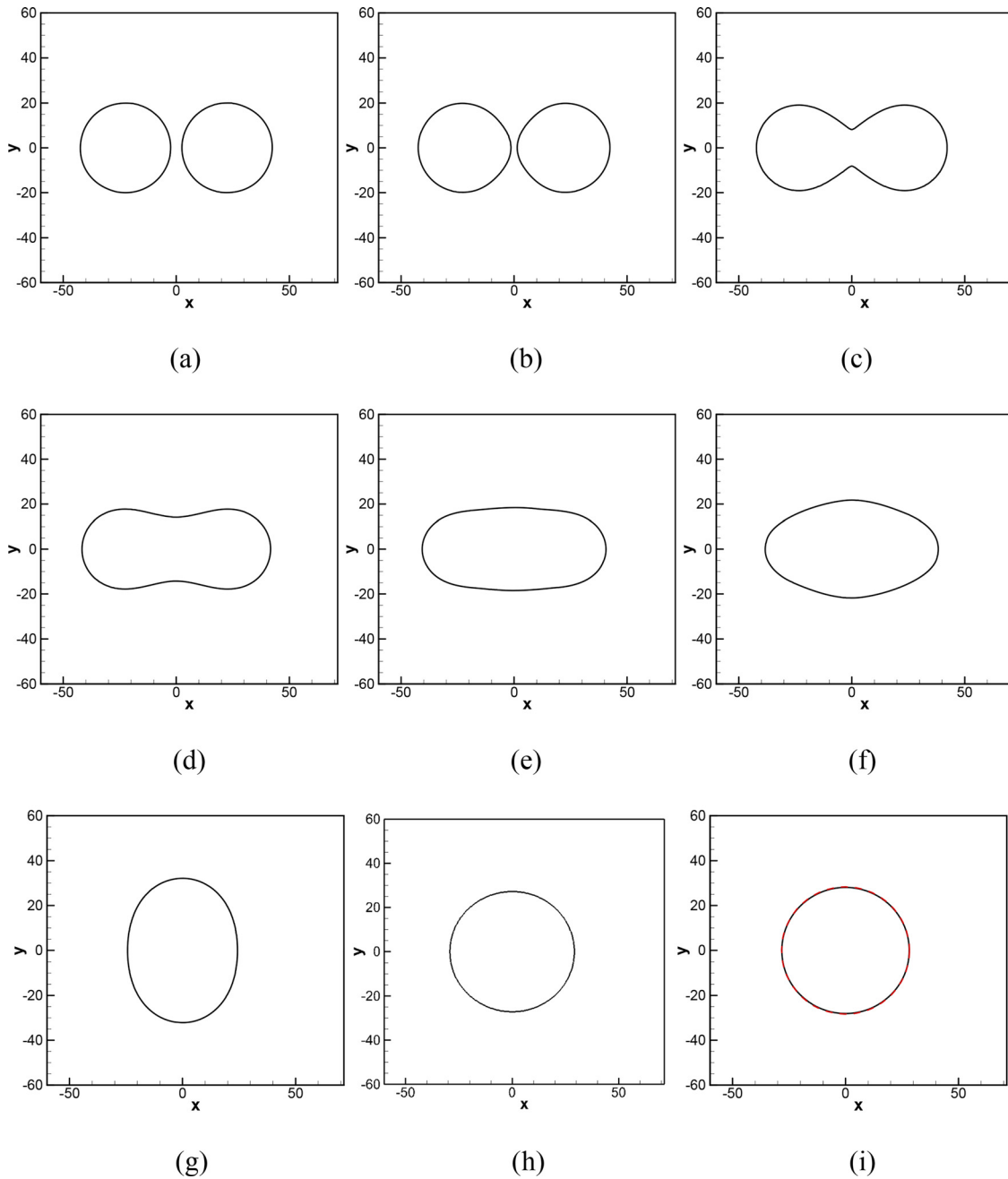
for fluid 1 and

FIG. 7. The interface changes of bubble shape at different time steps from (a) step $= 0$, (b) Step $= 1000$, (c) Step $= 2000$, (d) Step $= 3000$, (e) Step $= 4000$, (f) Step $= 5000$, (g) Step $= 10\,000$, (h) Step $= 20\,000$, (i) step $= 30\,000$ (red dotted line is the theoretical value; the black solid line is the numerical solution).

$$\bar{\psi}(x,y) = \frac{U_{\max}}{\omega} \frac{1}{\sinh^2(\beta) - \beta^2} \left\{ \omega y \sinh^2(\beta) \cosh(\omega y) \right.$$

$$\left. -0.5 \left[2\beta^2 - \omega y (\sinh(2\beta) - 2\beta) \right] \sinh(\omega y) \right\} \sin(\omega x), \quad (50)$$

$$\bar{T}(x,y) = \frac{\tilde{\kappa}(T_c - T_h)y + \tilde{\kappa}T_c b + T_h a}{a + \tilde{\kappa}b} + T_0 f(\alpha, \beta, \tilde{\kappa})$$

$$\times \left[\sinh(\alpha)\cosh(\omega y) - \tilde{\kappa}\sinh(\omega y)\cosh(\alpha) \right] \cos(\omega x) \quad (51)$$

for fluid 2. The parameters involved are given by

$$\tilde{\kappa} = \kappa_1 / \kappa_2, \quad (52)$$

$$\alpha = a\omega, \quad (53)$$

$$\beta = b\omega, \quad (54)$$

$$f(\alpha, \beta, \tilde{\kappa}) = 1 / \left(\tilde{\kappa}\sinh(\beta)\cosh\alpha + \sinh(\alpha)\cosh\beta \right), \quad (55)$$
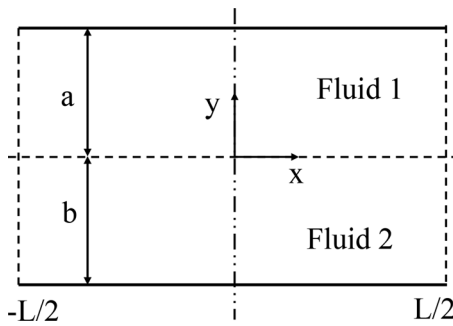
FIG. 8. The sketch of a heated microchannel with two superimposed fluids.

$$U_{\max} = -\left(\frac{T_0 \sigma_T}{\mu_B}\right) g(\alpha, \beta, \tilde{\kappa}) h(\alpha, \beta, \tilde{\mu}), \quad (56)$$

$$g(\alpha, \beta, \tilde{\kappa}) = \sinh(\alpha) f(\alpha, \beta, \tilde{\kappa}), \quad (57)$$

$$h(\alpha, \beta, \tilde{\mu})$$

$$= \frac{\left(\sinh^2(\alpha) - \alpha^2\right)\left(\sinh^2(\beta) - \beta^2\right)}{\tilde{\mu}\left(\sinh^2(\beta) - \beta^2\right)(\sinh(2\alpha) - 2\alpha) + \left(\sinh^2(\alpha) - \alpha^2\right)(\sinh(2\beta) - 2\beta)}. \quad (58)$$

Numerical simulations are carried out in a $[-80, 80] \times [-40, 40]$ domain with the initial heights of fluid layer $a = b = 40$. No-slip condition is imposed on the upper and lower walls, while the left and right boundaries are periodic. The temperature of the upper and lower walls is
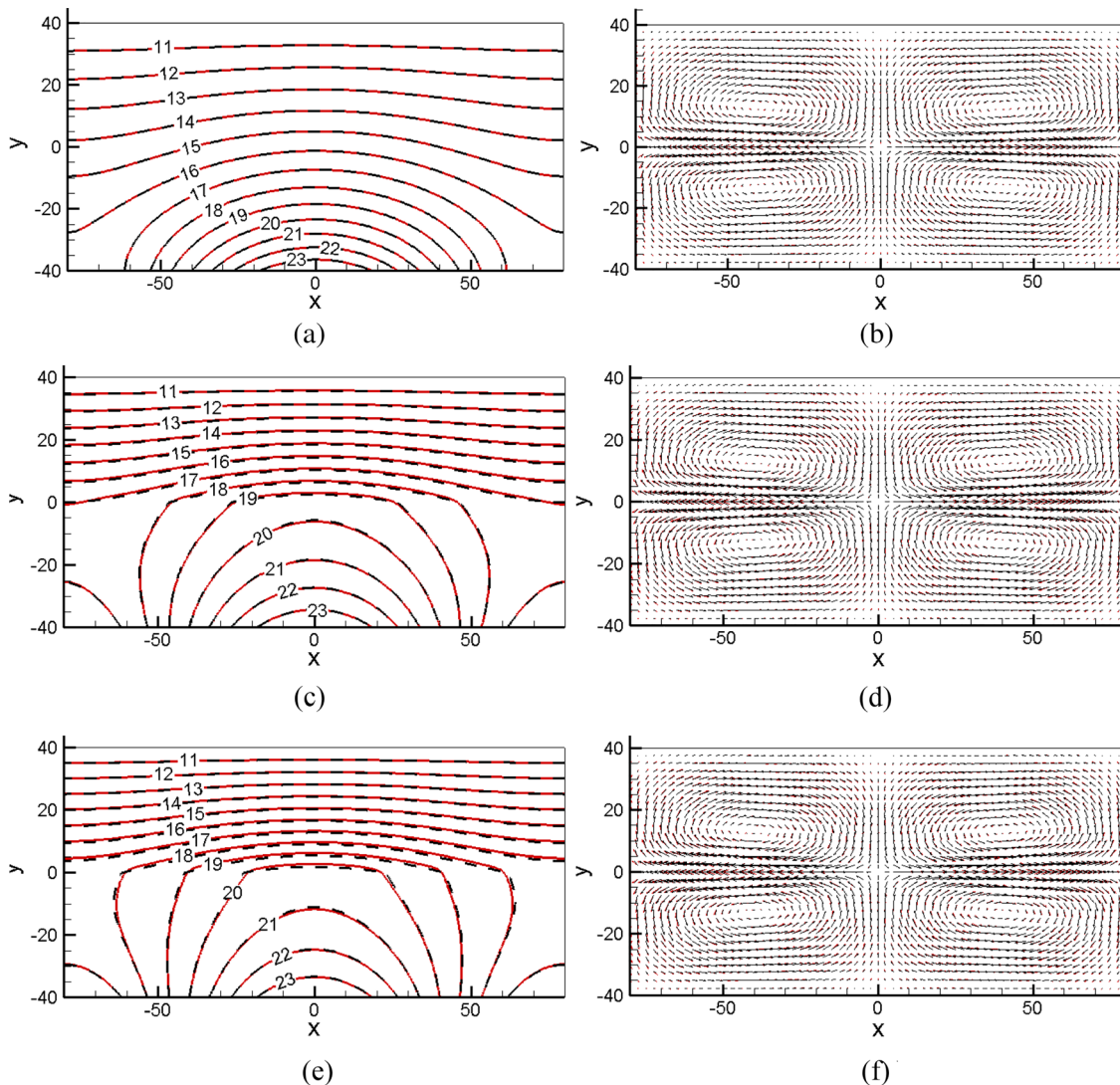

FIG. 9. At $t^* = 5$, temperature contours (a), (c), and (e) and velocity vector (b), (d), and (f) for the thermocapillary flows. The analytical and numerical results of the temperature are represented by black dashed and red solid lines, respectively. Similarly, the analytical and numerical results of the velocity vectors are denoted by black and red arrows. (a) Temperature contours at $\tilde{\kappa} = 1$. (b) Velocity vector at $\tilde{\kappa} = 1$. (c) Temperature contours at $\tilde{\kappa} = 0.2$. (d) Velocity vector at $\tilde{\kappa} = 0.2$. (e) Temperature contours at $\tilde{\kappa} = 0.1$. (f) Velocity vector at $\tilde{\kappa} = 0.1$.

TABLE V. The relative errors for the problem of a heated microchannel.

$\tilde{\kappa}$	Present		Liu et al.[40]		Qiao et al.[49]	
	E_T	E_U	E_T	E_U	E_T	E_U
1	6.95×10^{-5}	3.52×10^{-2}	2.25×10^{-4}	5.71×10^{-2}	$\cdots$	$\cdots$
0.2	2.64×10^{-3}	2.83×10^{-2}	5.23×10^{-3}	8.41×10^{-2}	5.069×10^{-3}	1.103×10^{-1}
0.1	4.14×10^{-3}	2.97×10^{-2}	$\cdots$	$\cdots$	$\cdots$	$\cdots$

specified through Eqs. (45) and (46), where $T_h = 20$ K, $T_0 = 4$ K, and $T_c = 10$ K. The fluid properties and other parameters adopted in the computation are chosen as $\rho_1 = \rho_2 = 1$ kg/m^3, $\mu_1 = \mu_2 = 0.2$ Pa · s, $c_{p1} = c_{p2} = 1$ J/(kg · K), $\kappa_2 = 0.2$ W/(m · K), $\kappa_1 = \tilde{\kappa}\kappa_2$, $\sigma_0 = 2.5 \times 10^{-2}$ N/m, $\sigma^T = -5 \times 10^{-4}$ N/m, and $M_0 = 0.05$. To investigate the dependency of the flow and temperature field on the thermal conductivity ratios, we consider three cases of $\tilde{\kappa} = 1$, $\tilde{\kappa} = 0.2$, and $\tilde{\kappa} = 0.1$. In each case, the system reaches a steady state after a dimensionless time $t^* = tU/L_r = 5$. The L^2-norm errors are defined by the following equations for the temperature and velocity, respectively, for quantitative validation of the present method:

$$E_T = \frac{\sum_x \|T(\mathbf{x}) - \bar{T}(\mathbf{x})\|_2}{\sum_x \|\bar{T}(\mathbf{x})\|_2}, \quad (59)$$

$$E_U = \frac{\sum_x \|\mathbf{u}(\mathbf{x}) - \bar{\mathbf{u}}(\mathbf{x})\|_2}{\sum_x \|\bar{\mathbf{u}}(\mathbf{x})\|_2}. \quad (60)$$

The analytical velocity $\bar{\mathbf{u}}(\mathbf{x})$ is deduced from the stream function $\bar{\Psi}(x, y)$ as follows:

$$\bar{u}(\mathbf{x}) = \frac{\partial \bar{\Psi}}{\partial y}, \quad \bar{v}(\mathbf{x}) = -\frac{\partial \bar{\Psi}}{\partial x}. \quad (61)$$

The left subplots in Fig. 9 show equispaced contours of the temperature for three cases with different thermal conductivity ratios. We observe that the results from the proposed method (black dashed lines) match well with the analytical distributions (red solid lines). The right subplot in Fig. 9 compares the velocity distribution from the present computation with the analytical solutions given by Eq. (61). The computed velocity vector matches well with the theoretical predictions and the thermocapillary convection intensifies with the reduction of thermal conductivity ratio. The relative L^2-norm errors for temperature and velocity are calculated according to Eqs. (59) and (60) and tabulated in Table V. Again, the proposed method proves to be much more accurate than the reference solutions for both the temperature and velocity predictions under thermocapillary effects.[49]

IV. TEST WITH COMPLEX CHANGE IN INTERFACIAL TOPOLOGY

In this section, we use two more numerical examples to assess the proposed method for more complex change in interfacial topology with large fluid property contrast and high Re.

A. Rising bubble

We examine the present solver by simulating a rising bubble in water with a large density ratio (1000) and viscosity ratio (100) under gravity $\mathbf{g}$ (0, −0.98) m/s^2. The computational domain $\Omega = [-0.5, 0.5] \times [0, 2]$ is shown in Fig. 10, which is covered by 3750 quadrilateral elements (50 elements in the x-direction and 75 elements in the y-direction). Following the problem setup as in Ref. 50, a bubble with a radius of R is initially placed in a rectangular area. The upper and lower boundaries are subject to no-slip conditions, and slip boundary conditions are applied on the left and right sides. The density and viscosity of air bubbles and environmental fluids are denoted by ρ_1, ρ_2, μ_1, μ_2, respectively. Choosing the diameter of the bubble $D = 2R = 0.5$ m as the characteristic length of the problem, the dimensionless parameter Reynolds number Re and Eotvos number Eo are, respectively, Re = $\rho_2 g^{0.5} D^{1.5} / \mu_2$,[50] Eo = $\rho_2 g D^2 / \sigma$, where the Eotvos number compares the force of gravity against the surface tension. Table VI gives the parameters adopted in the present computations. To quantitatively evaluate the results obtained, we introduce the following benchmark quantities:[50]

FIG. 10. Schematic diagram of a rising bubble.

TABLE VI. Relevant physical parameters and dimensionless values in the rising bubble test.

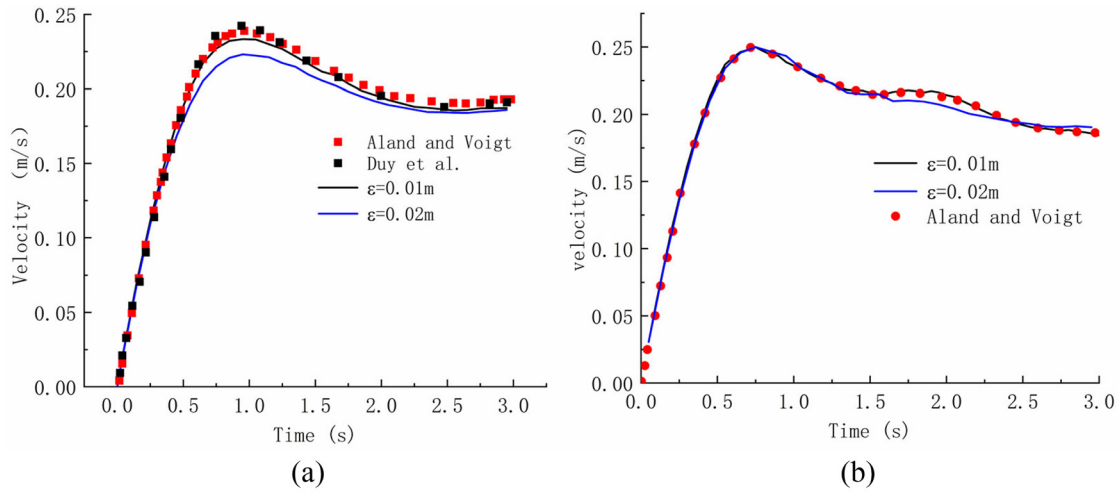| Case	Eo	Re	Σ (N/m)	ρ_1 (kg/m^3)	μ_1 (Pa · s)	ρ_2 (kg/m^3)	μ_2 (Pa · s)
A	10	35	24.5	100	1	1000	10
B	125		1.96	1	0.1	1000	10

FIG. 11. Comparison of the rising velocity V_c with benchmark solutions for the rising bubble for (a) case A and (b) case B.

1. Center of mass

$$y_c = \frac{\int_{\phi>0} y \, dx}{\int_{\phi>0} 1 \, dx},$$ (62)

where y is the vertical coordinate value.

2. Rise velocity

$$V_c = \frac{\int_{\phi>0} v \, dx}{\int_{\phi>0} 1 \, dx},$$ (63)

where v is the y-component of the velocity **u**.

We consider two cases with various parameters as shown in Table VI. With decrease in the interface width ε, the results from the present method converge and fit well with the reported data[51,52] as in Figs. 11–13. Particularly, Fig. 11 exhibits the evolution of rising speed with time. For case A, the bubble rising speed reaches the maximum and then gradually falls until a stable value; while for case B, the bubble speed continues to decrease after reaching the peak value. This is because the tail of the bubble gradually ruptures for case B as displayed in Fig. 14. Figure 12 plots the history of the position of the bubble's center of mass. We observe that the results from the present method agree well with the reference solution for both case A and case B. Figure 13 is a comparison of the results of the bubble shape and the literature at t = 3 s. The bubble shape of the two calculation examples compares favorably with the literature. Figure 14 shows the change process of the bubble at different
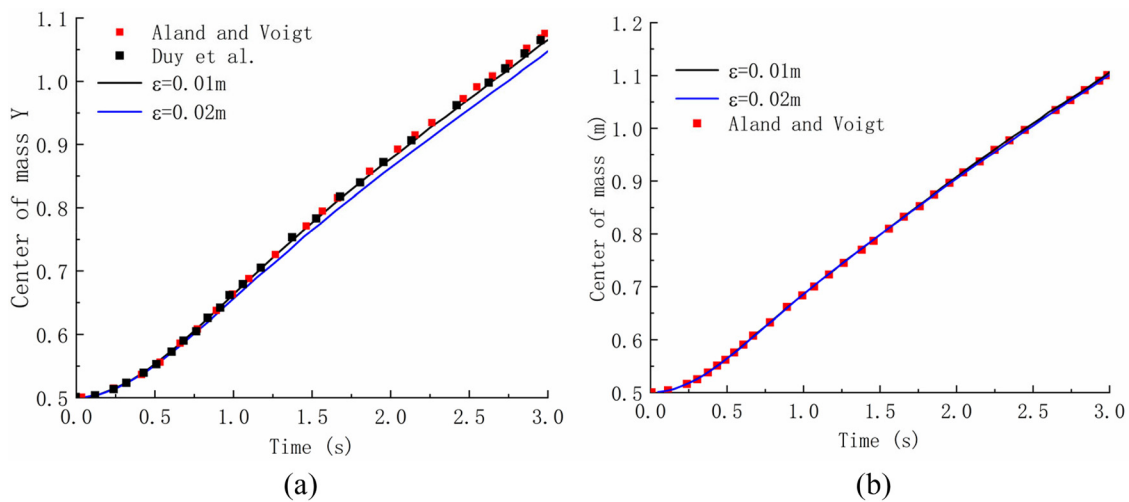

FIG. 12. History of the center of mass position y_c for (a) case A and (b) case B.
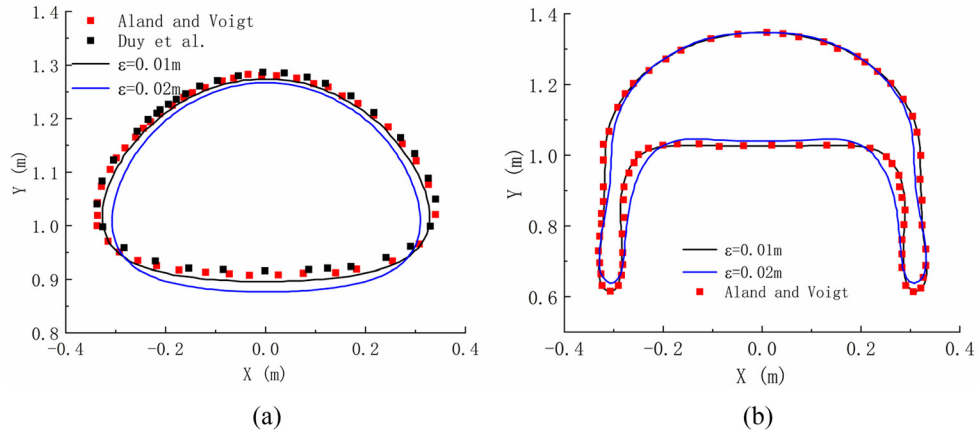
FIG. 13. Shape of the rising bubble at time $t = 3$ for (a) case A and (b) case B.
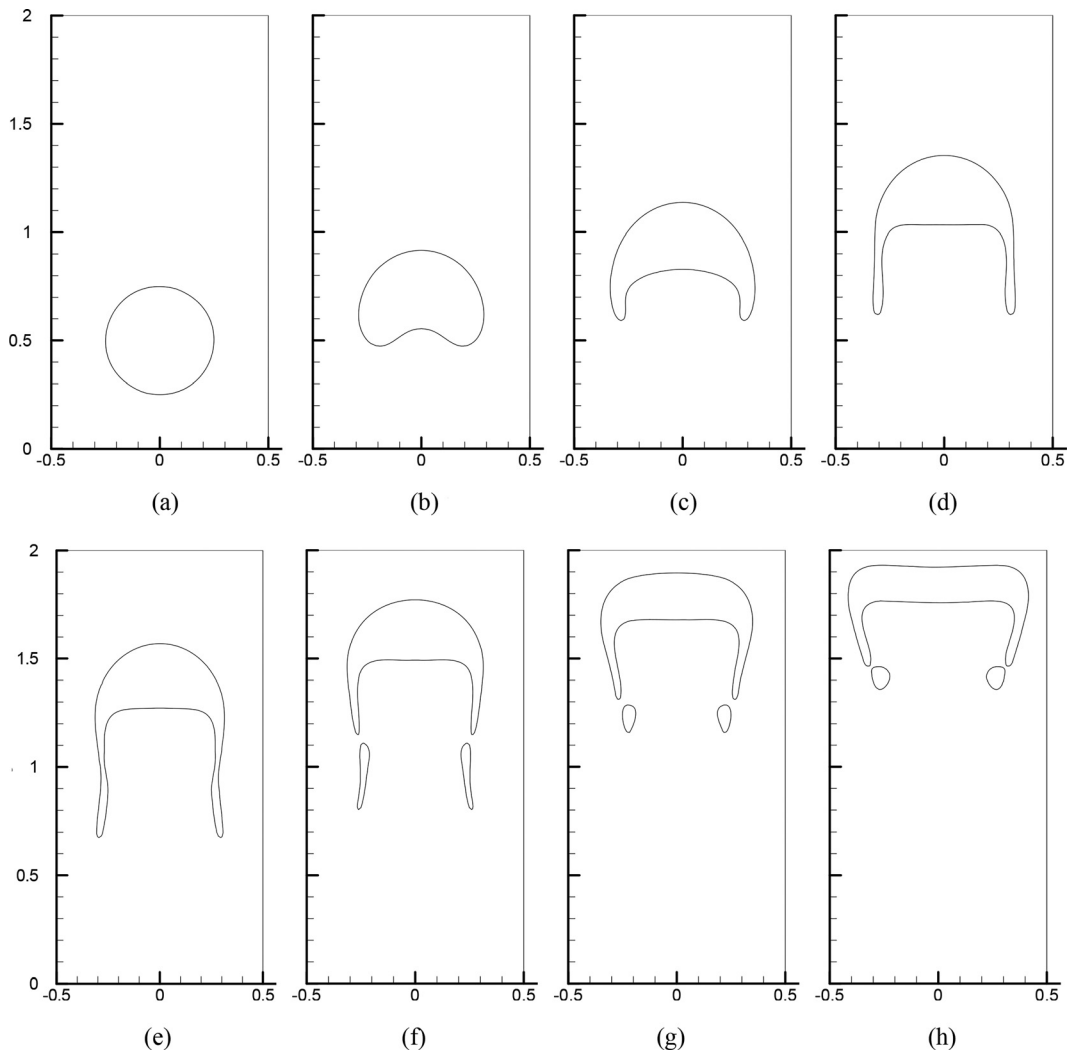

FIG. 14. The shape of rising bubbles at different times for case B, time changes from (a) $t = 0$ to (h) $t = 7$. (a) $t = 0$. (b) $t = 1$. (c) $t = 2$. (d) $t = 3$. (e) $t = 4$. (f) $t = 5$. (g) $t = 6$. (h) $t = 7$.

TABLE VII. Relevant physical parameters and dimensionless values in the Rayleigh–Taylor instability test.

Case	Re	At	ρ_1 (kg/m³)	μ_1 (Pa·s)	ρ_2 (kg/m³)	μ_2 (Pa·s)	g (m/s²)
A	256	0.5	3	300/256	1	300/256	0.01
B	3000	0.5	3	0.1	1	0.1	0.01

times for case B. The bubble gradually rises and small bubbles burst at the tail.

B. Rayleigh–Taylor instability

The unsteady Rayleigh–Taylor instability problem is finally performed to test the performance of the proposed method for computations with high Re, and thus cases at $Re = 256$ and $Re = 3000$ are considered here. When a slight disturbance is applied at the two-phase interface, the heavy fluid in the upper region will gradually invade the lighter fluid in the lower region under the action of gravity, and the disturbance at the interface develops and grows exponentially, and eventually becomes chaotic. We follow the case setup in Refs. 53, 54, and 47, the computational domain has dimensions $\Omega = [0, L/2] \times [-2L, 2L]$, which is resolved by 3200 quadrilateral elements (20 elements in the x-direction and 160 elements in the y-direction), and L (100 m) is the characteristic length. The upper part of the computational domain contains the heavy fluid ($\rho_1 = 3$ kg/m³), and the lower part contains the light fluid ($\rho_2 = 1$ kg/m³). A slight disturbance is applied at the interface with disturbance function $h = -0.1 \cos(2\pi x)$, and the phase variable is initially distributed as follows:

$$\phi(t = 0) = \tanh\left(\frac{1}{\sqrt{2}\varepsilon}(y - h)\right). \quad (64)$$

FIG. 16. The location of spike and bubble of Rayleigh–Taylor instability at different times for the case A.

The initial velocity field is stationary. The surface tension is switched off in the present test. No-slip conditions are applied for the upper and lower boundaries, and slip conditions are imposed at the left and right sides. Two dimensionless numbers are used in this test: the Reynolds number $Re = \rho_1 LU/\mu_1$ and Atwood number $At = (\rho_1 - \rho_2)/(\rho_1 + \rho_2)$, where μ_1 is the viscosity of the heavy fluid and U is the characteristic velocity $U = \sqrt{gL}$. The time is scaled by $\sqrt{L/g}$.[55] This test considered the process of Rayleigh–Taylor instability under the influence of two different parameters. We consider two cases with the detailed parameter setting as given in Table VII.
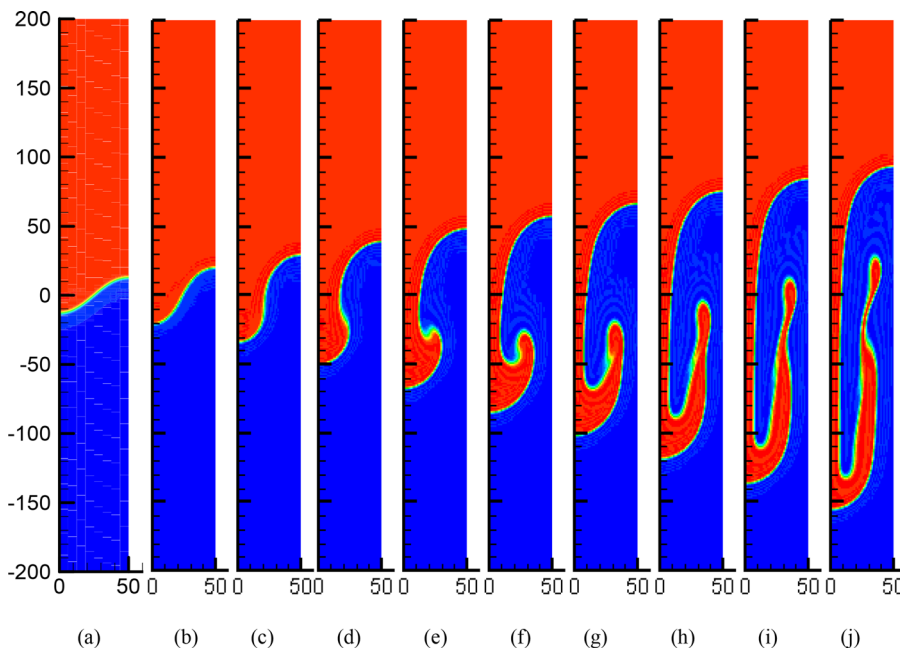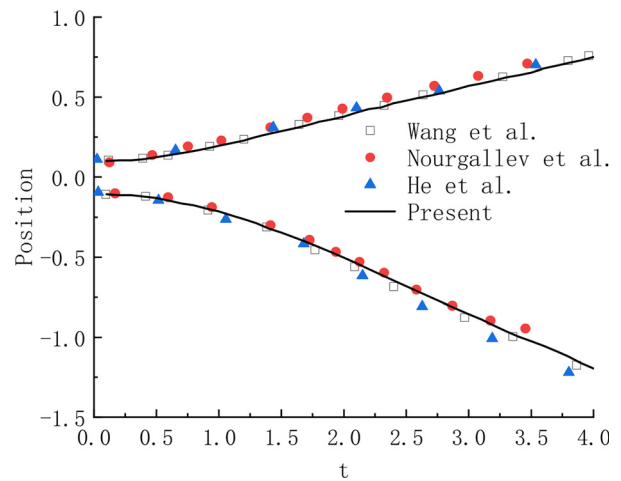

FIG. 15. Interfacial dynamics of the Rayleigh–Taylor instability at different times for the case of density ratio = 3 and Re = 256. Time changes from (a) t = 0.5 to (j) t = 5 with 0.5 increment.
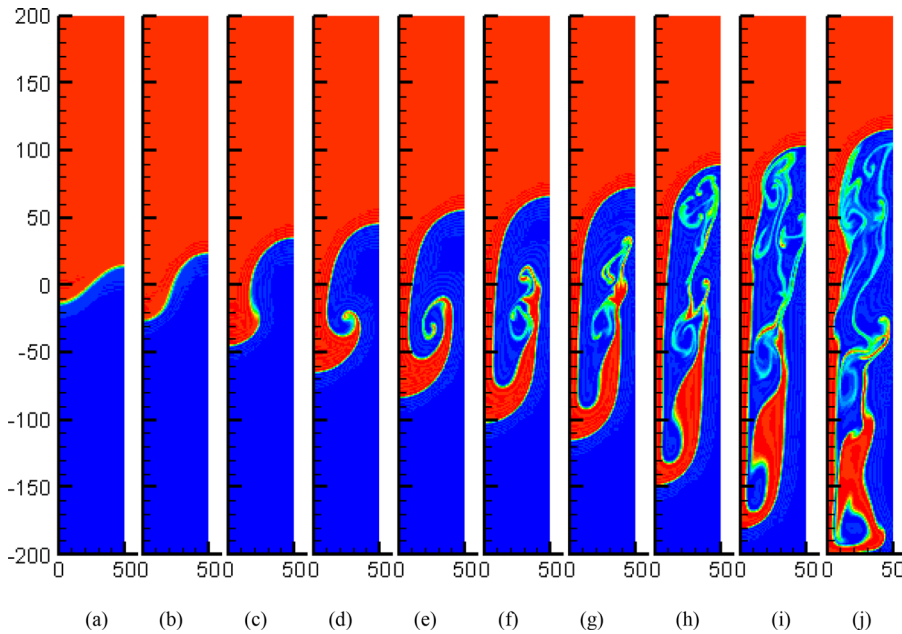
FIG. 17. Interfacial dynamics of the Rayleigh–Taylor instability at different times for the case of density ratio = 3 and $Re = 3000$ [time changes from (a) t = 0.5 to (j) t = 5 with 0.5 increment].
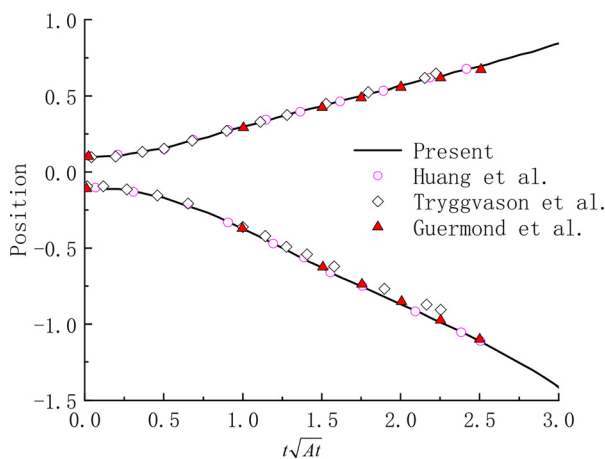
FIG. 18. Location of the spike and bubble of the Rayleigh–Taylor instability at different times for case B.

Figure 15 demonstrates the evolution of the interface over time at $Re = 256$ (case A). Under the influence of the initial interface disturbance and the gravitational effects, the heavy fluid falls down from the left side and the light fluid climbs upward from the right side, forming a spike and bubble, respectively. Figure 16 shows the positions of the spikes and bubbles in the y-direction at different times. It can be seen that the results obtained here are in good agreement with the reference results by Wang et al.[47] and He et al.[56] Similarly, the interfacial dynamics for case B with a density ratio 3 and $Re = 3000$ is shown in Fig. 17. With time, the interface becomes more and more disordered. Additionally, Fig. 18 compares the positions of the spike and bubble from the proposed method with the published results, which exhibit

excellent agreements with the studies of Huang et al.,[22] Tryggvason,[57] and Guermond and Quartapelle.[53]

V. CONCLUSION

In this work, a spectral element-based phase field method is proposed for two-phase flows with large fluid property contrast and at high Re. We propose to use the Newton–Raphson method to resolve the high-order nonlinear feature of the Cahn–Hilliard equation, and the time-stepping scheme is applied for the Navier–Stokes equation to improve the stability and convergence efficiency. Furthermore, the interfacial force is represented by the continuum surface force model to include contributions from the tangential component of the surface tension, i.e., the Marangoni stress.

Numerical tests, including Zalesak's disk rotation, reversed single vortex flow, bubbles merging, thermocapillary flows in a heated microchannel, as well as rising bubble and Rayleigh–Taylor instability, are conducted to systematically validate the proposed method in terms of the interface capture accuracy and versatility for practical two-phase flows. The proposed method appears to be much more accurate than the usual second-order method and other high-order methods by quantitatively referring to the analytical solutions, and the present method obeys mass conservation better than the results reported in the literature. Tests with more complex interfacial dynamics further prove its robustness for two-phase flows with large density and viscosity contrast and at high Re.

AUTHOR DECLARATIONS
Conflict of Interest

We declare that we do not have any commercial or associative interest that represents a conflict of interest in connection with the work submitted.

DATA AVAILABILITY

The data that support the findings of this study are available from the corresponding author upon reasonable request.

APPENDIX: SPECTRAL ELEMENT METHOD

We detail spatial discretization in the context of the spectral element method. Consider the following two-dimensional Poisson-type problem:

$$\begin{cases} -\nabla^2 u + \alpha(x,y)u = f(x,y), & \Omega = [x_a, x_b] \times [y_a, y_b], \\ u|_\Gamma = g_1(x,y), \\ \dfrac{\partial u}{\partial \mathbf{n}}\bigg|_\Gamma = g_2(x,y), \end{cases} \quad (A1)$$

where u denotes an unknown function. $\alpha(x,y)$, $g_1(x,y)$, $g_2(x,y)$, and $f(x,y)$ are given functions, respectively, on the domain Ω or along the boundary Γ. For $\alpha(x,y) = 0$ and $f(x,y) \neq 0$, Eq. (A1) is the Poisson equation. When $\alpha(x,y) \neq 0$, Eq. (A1) is the Helmholtz equation. The computational domain Ω is divided into Ne non-overlapped elements $\Omega^i = [x_i, x_{i+1}] \times [y_i, y_{i+1}]$. By the coordinate transformation $\xi = 2\frac{x-x_i}{x_{i+1}-x_i} - 1$ and $\eta = 2\frac{y-y_i}{y_{i+1}-y_i} - 1$, the subdomains Ω^i are mapped to a standard computation domain Ω^e: $[-1,1] \times [-1,1]$. The function u and f in each element Ω^i are expanded as follows:

$$u^i(\xi, \eta) = \sum_{j=0}^{N_\xi} \sum_{k=0}^{N_\eta} u^i(\xi_i, \eta_i) h_j^i(\xi) h_k^i(\eta), \quad (A2)$$

$$f^i(\xi, \eta) = \sum_{j=0}^{N_\xi} \sum_{k=0}^{N_\eta} f^i(\xi_i, \eta_i) h_j^i(\xi) h_k^i(\eta), \quad (A3)$$

where N_ξ-degree and N_η-degree Legendre polynomials are used, respectively, in the x- and y-directions. $u^i(\xi_i, \eta_i)$ represents the value of u on node (ξ_i, η_i). $h_j(\xi_i)$ and $h_k(\eta_i)$ are polynomials with corresponding to the Legend–Gauss–Lobatto points. A test function q is defined in the polynomial space V_N with the specified boundary conditions of Eq. (A1). After multiplying Eq. (A1) by the conjugate of q and integrating by parts in Ω^i, its Galerkin formation is obtained: find $u \in H_0^1(\Omega^i)$, such that

$$\int_{\Omega^i} \frac{\partial u}{\partial x} \frac{\partial \bar{q}}{\partial x} dxdy + \int_{\Omega^i} \frac{\partial u}{\partial y} \frac{\partial \bar{q}}{\partial y} dxdy + \int_{\Omega^i} au\bar{q} dxdy$$
$$= \int_{\Omega^i} f\bar{q} dxdy + \int_{\Gamma^i} g_2 \bar{q} dS, \quad (A4)$$

where $H_0^1(\Omega^i)$ is the Sobolev space. Let

$$q^i(\xi, \eta) = \sum_{m=0}^{N_\xi} \sum_{n=0}^{N_\eta} q^i(\xi_m, \eta_n) h_m^i(\xi) h_n^i(\eta). \quad (A5)$$

Henceforth, $u^i(\xi, \eta)$ and $f^i(\xi, \eta)$ are abbreviated to u_{jk} and f_{ij} for convenience. According to Eqs. (A2)–(A5) and without considering the Neumann boundary conditions, we obtain the discrete linear equations in Ω^i as follows:

$$\sum_{j=0}^{N_\xi} \sum_{k=0}^{N_\eta} u_{jk}(A_{jkmn} + \alpha B_{jkmn}) = \sum_{j=0}^{N_\xi} \sum_{k=0}^{N_\eta} f_{jk} B_{jkmn}, \quad (A6)$$

where

$$A_{jkmn} = A_{jm}B_{kn} + B_{jm}A_{kn}, \quad (A7)$$
$$B_{jkmn} = B_{jm}B_{kn}, \quad (A8)$$
$$\mathrm{N}_{jkmn}^{\mathrm{x}} = \mathrm{N}_{jm}B_{kn}, \quad (A9)$$
$$\mathrm{N}_{jkmn}^{\mathrm{y}} = B_{jm}\mathrm{N}_{kn}, \quad (A10)$$

$$A_{jm} = \int_{x_i}^{x_{i+1}} \frac{\partial h_j(\xi)}{\partial x} \frac{\partial h_m(\xi)}{\partial x} dx, \quad (A11)$$

$$A_{kn} = \int_{y_i}^{y_{i+1}} \frac{\partial h_k(\eta)}{\partial y} \frac{\partial h_n(\eta)}{\partial y} dy, \quad (A12)$$

$$B_{jm} = \int_{x_i}^{x_{i+1}} h_j(\xi) h_m(\xi) dx, \quad (A13)$$

$$B_{kn} = \int_{y_i}^{y_{i+1}} h_k(\eta) h_n(\eta) dy, \quad (A14)$$

$$N_{jm} = \int_{x_i}^{x_{i+1}} \frac{\partial \mathrm{h}_j(\xi)}{\partial x} \mathrm{h}_m(\xi) dx, \quad (A15)$$

$$N_{kn} = \int_{y_i}^{y_{i+1}} \frac{\partial \mathrm{h}_k(\eta)}{\partial y} h_n^\eta(\eta) dy. \quad (A16)$$

According to the finite element method,[58] the global stiffness matrix can be constructed by the element stiffness matrix resulting from Eqs. (A6)–(A16). Finally, by solving the linear equations with given boundary conditions, we can obtain the value on each node. More information about the spectral element method can be found in our previous paper[59] or some reputed books.[60–62]

REFERENCES

[1] T. Tao and Q. Zhonghua, "Efficient numerical methods for phase-field equations," Sci. Sin. Math. **50**, 775 (2020).

[2] L. T. Liu, X. B. Chen, W. Q. Zhang, and A.-M. Zhang, "Study on the transient characteristics of pulsation bubble near a free surface based on finite volume method and front tracking method," Phys. Fluids **32**, 052107 (2020).

[3] S.-I. Sohn, "A computational model of the swimming dynamics of a fish-like body in two dimensions," Phys. Fluids **33**, 121902 (2021).

[4] S. B. Q. Tran, Q. T. Le, F. Y. Leong, and D. V. Le, "Modeling deformable capsules in viscous flow using immersed boundary method," Phys. Fluids **32**, 093602 (2020).

[5] M. P. Borthakur, G. Biswas, and D. Bandyopadhyay, "Dynamics of deformation and pinch-off of a migrating compound droplet in a tube," Phys. Rev. E **97**, 043112 (2018).

[6] A. M. P. Boelens and J. J. de Pablo, "Generalised Navier boundary condition for a volume of fluid approach using a finite-volume method," Phys. Fluids **31**, 021203 (2019).

[7] Z. Che, Y. F. Yap, and T. Wang, "Flow structure of compound droplets moving in microchannels," Phys. Fluids **30**, 012114 (2018).

[8] S. Santra, S. Das, and S. Chakraborty, "Electrically modulated dynamics of a compound droplet in a confined microfluidic environment," J. Fluid Mech. **882**, A23 (2020).

[9] S. Santra, D. P. Panigrahi, S. Das, and S. Chakraborty, "Shape evolution of compound droplet in combined presence of electric field and extensional flow," Phys. Rev. Fluids **5**, 063602 (2020).

[10]P. Yue, J. J. Feng, C. Liu, and J. I. E. Shen, "A diffuse-interface method for simulating two-phase flows of complex fluids," J. Fluid Mech. **515**, 293 (2004).

[11]J. D. Van der Waals, "The thermodynamic theory of capillarity under the hypothesis of a continuous variation of density," J. Stat. Phys. **20**, 200 (1979).

[12]J. W. Cahn and J. E. Hilliard, "Free energy of a nonuniform system. I. Interfacial free energy," J. Chem. Phys. **28**, 258 (1958).

[13]J. W. Cahn, "Free energy of a nonuniform system. II. Thermodynamic basis," J. Chem. Phys. **30**, 1121 (1959).

[14]J. W. Cahn and J. E. Hilliard, "Free energy of a nonuniform system. III. Nucleation in a two-component incompressible fluid," J. Chem. Phys. **31**, 688 (1959).

[15]O. J. J. Ronsin, D. Jang, H. J. Egelhaaf, C. J. Brabec, and J. Harting, "A phase-field model for the evaporation of thin film mixtures," Phys. Chem. Chem. Phys. **22**, 6638 (2020).

[16]S. Santra, D. Sen, S. Das, and S. Chakraborty, "Electrohydrodynamic interaction between droplet pairs in a confined shear flow," Phys. Fluids **31**, 032005 (2019).

[17]L. Qiao, Z. Zeng, and H. Xie, "Phase-field-based finite volume method for simulating thermocapillary flows," Procedia Eng. **126**, 507 (2015).

[18]H. Liu, Y. Lu, S. Li, Y. Yu, and K. C. Sahu, "Deformation and breakup of a compound droplet in three-dimensional oscillatory shear flow," Int. J. Multiphase Flow **134**, 103472 (2021).

[19]H. Liang, B. Shi, Z. Guo, and Z. Chai, "Phase-field-based multiple-relaxation-time lattice Boltzmann model for incompressible multiphase flows," Phys. Rev. E **89**, 053320 (2014).

[20]H. L. Wang, Z. H. Chai, B. C. Shi, and H. Liang, "Comparative study of the lattice Boltzmann models for Allen–Cahn and Cahn–Hilliard equations," Phys. Rev. E **94**, 033304 (2016).

[21]S. Dong and J. Shen, "A time-stepping scheme involving constant coefficient matrices for phase-field simulations of two-phase incompressible flows with large density ratios," J. Comput. Phys. **231**, 5788 (2012).

[22]Z. Huang, G. Lin, and A. M. Ardekani, "Consistent, essentially conservative and balanced-force phase-field method to model incompressible two-phase flows," J. Comput. Phys. **406**, 109192 (2020).

[23]H. W. Zheng, C. Shu, and Y. T. Chew, "Lattice Boltzmann interface capturing method for incompressible flows," Phys. Rev. E **72**, 056705 (2005).

[24]A. Fakhari and M. H. Rahimian, "Phase-field modeling by the method of lattice Boltzmann equations," Phys. Rev. E **81**, 036707 (2010).

[25]Y. Q. Zu and S. He, "Phase-field-based lattice Boltzmann model for incompressible binary fluid systems with density and viscosity contrasts," Phys. Rev. E **87**, 043301 (2013).

[26]Y. Wang, C. Shu, H. B. Huang, and C. J. Teo, "Multiphase lattice Boltzmann flux solver for incompressible multiphase flows with large density ratio," J. Comput. Phys. **280**, 404 (2015).

[27]P. Yue, "Thermodynamically consistent phase-field modelling of contact angle hysteresis," J. Fluid Mech. **899**, A15 (2020).

[28]Y. Hu, "A diffuse interface–lattice Boltzmann model for surfactant transport on an interface," Appl. Math. Lett. **111**, 106614 (2021).

[29]C. Ma, J. Wu, and T. Zhang, "A high order spectral difference-based phase field lattice Boltzmann method for incompressible two-phase flows," Phys. Fluids **32**, 122113 (2020).

[30]L. Q. Chen and J. Shen, "Applications of semi-implicit Fourier-spectral method to phase field equations," Comput. Phys. Commun. **108**, 147 (1998).

[31]J. Shen and X. Yang, "Numerical approximations of Allen–Cahn and Cahn–Hilliard equations," Discrete Contin. Dyn. Syst. **28**, 1669 (2010).

[32]H. Shi and Y. Li, "Local discontinuous Galerkin methods with implicit-explicit multistep time-marching for solving the nonlinear Cahn–Hilliard equation," J. Comput. Phys. **394**, 719 (2019).

[33]K. Park, M. Fernandino, C. A. Dorao, and M. Gerritsma, "The least-squares spectral element method for phase-field models for isothermal fluid mixture," Comput. Math. Appl. **74**, 1981 (2017).

[34]J. Manzanero, G. Rubio, D. A. Kopriva, E. Ferrer, and E. Valero, "A free–energy stable nodal discontinuous Galerkin approximation with summation–by–parts property for the Cahn–Hilliard equation," J. Comput. Phys. **403**, 109072 (2020).

[35]J. Manzanero, G. Rubio, D. A. Kopriva, E. Ferrer, and E. Valero, "Entropy–stable discontinuous Galerkin approximation with summation–by–parts property for the incompressible Navier–Stokes/Cahn–Hilliard system," J. Comput. Phys. **408**, 109363 (2020).

[36]J. Shen and X. Yang, "A phase-field model and its numerical approximation for two-phase incompressible flows with different densities and viscosities," SIAM J. Sci. Comput. **32**, 1159 (2010).

[37]J. Shen and X. Yang, "Energy stable schemes for Cahn–Hilliard phase-field model of two-phase incompressible flows," Chin. Ann. Math., Ser. B **31**, 743 (2010).

[38]X. Zheng, H. Babaee, S. Dong, C. Chryssostomidis, and G. E. Karniadakis, "A phase-field method for 3D simulation of two-phase heat transfer," Int. J. Heat Mass Transfer **82**, 282 (2015).

[39]H. Liu, A. J. Valocchi, Y. Zhang, and Q. Kang, "Lattice Boltzmann phase-field modeling of thermocapillary flows in a confined microchannel," J. Comput. Phys. **256**, 334 (2014).

[40]H. Liu, A. J. Valocchi, Y. Zhang, and Q. Kang, "Phase-field-based lattice Boltzmann finite-difference model for simulating thermocapillary flows," Phys. Rev. E **87**, 013010 (2013).

[41]P. K. Kristensen and E. Martínez-Pañeda, "Phase field fracture modelling using quasi-Newton methods and a new adaptive step scheme," Theor. Appl. Fract. Mech. **107**, 102446 (2020).

[42]V. Badalassi, H. Ceniceros, and S. Banerjee, "Computation of multiphase systems with phase field models," J. Comput. Phys. **190**, 371 (2003).

[43]J. Shen and X. Yang, "An efficient moving mesh spectral method for the phase-field model of two-phase flows," J. Comput. Phys. **228**, 2978 (2009).

[44]M. Geier, A. Fakhari, and T. Lee, "Conservative phase-field lattice Boltzmann model for interface tracking equation," Phys. Rev. E **91**, 063309 (2015).

[45]H. W. Zheng, C. Shu, and Y.-T. Chew, "A lattice Boltzmann model for multiphase flows with large density ratio," J. Comput. Phys. **218**, 353 (2006).

[46]T. Zhang, J. Wu, and X. Lin, "An interface-compressed diffuse interface method and its application for multiphase flows," Phys. Fluids **31**, 122102 (2019).

[47]Y. Wang, C. Shu, J. Y. Shao, J. Wu, and X. D. Niu, "A mass-conserved diffuse interface method and its application for incompressible multiphase flows with large density ratio," J. Comput. Phys. **290**, 336 (2015).

[48]B. Pendse and A. Esmaeeli, "An analytical solution for thermocapillary-driven convection of superimposed fluids at zero Reynolds and Marangoni numbers," Int. J. Therm. Sci. **49**, 1147 (2010).

[49]L. Qiao, Z. Zeng, H. Xie, L. Zhang, L. Wang, and Y. Lu, "Modeling thermocapillary migration of interfacial droplets by a hybrid lattice Boltzmann finite difference scheme," Appl. Therm. Eng. **131**, 910 (2018).

[50]S. Hysing, S. Turek, D. Kuzmin, N. Parolini, E. Burman, S. Ganesan, and L. Tobiska, "Quantitative benchmark computations of two-dimensional bubble dynamics," Int. J. Numer. Methods Fluids **60**, 1259 (2009).

[51]S. Aland and A. Voigt, "Benchmark computations of diffuse interface models for two-dimensional bubble dynamics," Int. J. Numer. Methods Fluids **69**, 747 (2012).

[52]T.-N. Duy, V.-T. Nguyen, T.-H. Phan, and W.-G. Park, "An enhancement of coupling method for interface computations in incompressible two-phase flows," Comput. Fluids **214**, 104763 (2021).

[53]J. L. Guermond and L. Quartapelle, "A projection FEM for variable density incompressible flows," J. Comput. Phys. **165**, 167 (2000).

[54]G. Fu, "A divergence-free HDG scheme for the Cahn–Hilliard phase-field model for two-phase incompressible flow," J. Comput. Phys. **419**, 109671 (2020).

[55]Y. Hu, Q. He, D. Li, Y. Li, and X. Niu, "On the total mass conservation and the volume preservation in the diffuse interface method," Comput. Fluids **193**, 104291 (2019).

[56]X. Y. He, S. Chen, and R. Zhang, "A lattice Boltzmann scheme for incompressible multiphase flow and its application in simulation of Rayleigh–Taylor instability," J. Comput. Phys. **152**, 642 (1999).

[57]G. Tryggvason, "Numerical simulations of the Rayleigh–Taylor instability," J. Comput. Phys. **75**, 253 (1988).

[58]I. M. Smith and D. V. Griffiths, *Programming the Finite Element Method* (John Wiley & Sons, Inc., 1998).

[59]Z. Qiu, Z. Zeng, H. Mei, L. Li, L. Yao, and L. Zhang, "A Fourier–Legendre spectral element method in polar coordinates," J. Comput. Phys. **231**, 666 (2012).

[60]J. Shen, T. Tang, and L.-L. Wang, *Spectral Methods: Algorithms, Analysis and Applications* (Springer Publishing Company, Incorporated, 2011).

[61]C. Canuto, M. Y. Hussaini, A. Quarteroni, and T. A. Zang, *Spectral Methods: Evolution to Complex Geometries and Applications to Fluid Dynamics* (Springer Science & Business Media, 2007).

[62]G. E. Karniadakis and S. J. Sherwin, *Spectral/hp Element Methods for CFD* (Oxford University Press, 1999).